


## MATERIALS SCIENCE

# A highly alkaline-stable metal oxide@metal–organic framework composite for high-performance electrochemical energy storage

Shasha Zheng <sup>1</sup>, Qing Li<sup>1</sup>, Huaiguo Xue<sup>1</sup>, Huan Pang<sup>1,\*</sup> and Qiang Xu<sup>1,2,\*</sup>

## ABSTRACT

Most metal–organic frameworks (MOFs) hardly maintain their physical and chemical properties after exposure to alkaline aqueous solutions, thus precluding their use as potential electrode materials for electrochemical energy storage devices. Here, we present the design and synthesis of a highly alkaline-stable metal oxide@MOF composite,  $\text{Co}_3\text{O}_4$  nanocube@Co-MOF ( $\text{Co}_3\text{O}_4$ @Co-MOF), via a controllable and facile one-pot hydrothermal method under highly alkaline conditions. The obtained composite possesses exceptional alkaline stability, retaining its original structure in 3.0 M KOH for at least 15 days. Benefitting from the exceptional alkaline stability, unique structure, and larger surface area, the  $\text{Co}_3\text{O}_4$ @Co-MOF composite shows a specific capacitance as high as  $1020 \text{ F g}^{-1}$  at  $0.5 \text{ A g}^{-1}$  and a high cycling stability with only 3.3% decay after 5000 cycles at  $5 \text{ A g}^{-1}$ . The as-constructed solid-state flexible device exhibits a maximum energy density of  $21.6 \text{ mWh cm}^{-3}$ .

**Keywords:** metal–organic framework, metal oxide, composite, electrochemical energy storage, flexible supercapacitor

## INTRODUCTION

Metal–organic frameworks (MOFs) are formed via self-assembly of metal ions and organic linkers [1–3]. Due to their superior properties, such as their large surface area, high porosity and structure tunability, MOFs have recently emerged as one type of important porous materials and have attracted intense interest in many fields, such as gas storage and separation [4–7], catalysis [8–11] and energy storage [12–15]. Nevertheless, MOFs still have a few weak points, which impede the use of their full potential to a great extent. For example, most MOFs manifest inferior properties for electrical conduction and have limited chemical stability (in water, especially alkaline conditions), preventing them from exhibiting their best performance in the field of electrochemistry [16–19]. Fortunately, hybridizing MOFs with a variety of functional materials to generate MOF composites can integrate the merits and mitigate the shortcomings of both parent materials [20–23].

Metal oxide nanomaterials with controllable shape, size, crystallinity and functionality are widely

applied in many fields [24–27]. Because of their high theoretical specific capacitance, low cost and great reversibility, they are considered ideal pseudocapacitive electrode materials, but they have high surface energies and are prone to aggregation, leading to loss of the pseudocapacitive performance [28–30]. In addition, metal oxides usually display only small surface areas, which has largely restricted their use as electrode materials for electrochemical energy storage [31,32]. Consequently, finding a cost-effective method to increase the specific surface areas of metal oxides is crucial for achieving high pseudocapacitive activity.

Here, we report a strategy to integrate the advantages of both metal oxides and MOFs by hybridizing metal oxides with MOFs having large surface areas, in which each component retains its own identity while contributing extraordinary characteristics to the whole system [33,34]. MOFs with high surface areas provide appropriate spaces for the electrochemical reaction and intercalation/de-intercalation of cations (e.g.  $\text{Li}^+$ ,  $\text{Na}^+$ ,  $\text{K}^+$  and  $\text{H}^+$ ) during energy storage processes

<sup>1</sup>School of Chemistry and Chemical Engineering, and Institute for Innovative Materials and Energy, Yangzhou University, Yangzhou 225009, China and

<sup>2</sup>AIST-Kyoto University Chemical Energy Materials Open Innovation Laboratory, National Institute of Advanced Industrial Science and Technology, Kyoto 606-8501, Japan

\*Corresponding authors. E-mails: huanpangchem@hotmail.com; panghuan@yzu.edu.cn; q.xu@aist.go.jp; qxu@chem@yzu.edu.cn

Received 11 June 2019; Revised 1 August 2019;

Accepted 20 August 2019

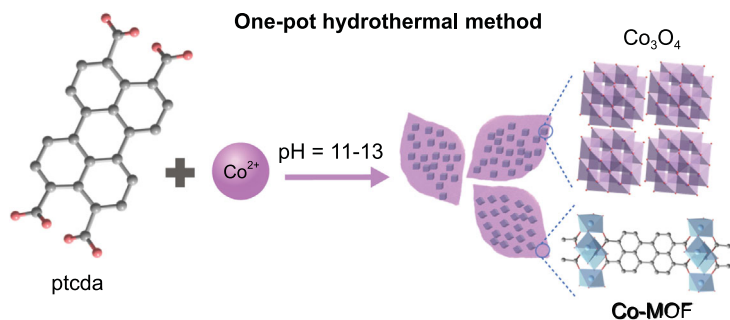


**Figure 1.** Schematic illustration of one-pot hydrothermal synthesis of  $\text{Co}_3\text{O}_4$ @Co-MOF composite.

[13,35,36], while the presence of metal oxides effectively increases redox active sites [37–39]. We have successfully synthesized Co-MOF sheet ( $\text{Co-MOF}$ ,  $\text{Co}_2(\text{ptcda})\cdot 2\text{H}_2\text{O}$ ,  $\text{ptcda}$  = perylene-3,4,9,10-tetracarboxylic dianhydride) through a simple one-pot hydrothermal method from the coordination of  $\text{ptcda}$  and  $\text{Co}^{2+}$ . Interestingly,  $\text{Co}_3\text{O}_4$  nanocubes grow on the surface of the Co-MOF sheet, forming the  $\text{Co}_3\text{O}_4$ @Co-MOF composite at  $\text{pH} = 11\text{--}13$ , which shows exceptional alkaline stability in 3.0 M KOH. Using the  $\text{Co}_3\text{O}_4$ @Co-MOF composite as the electrode for a supercapacitor, the specific capacitance reaches  $1020 \text{ F g}^{-1}$  at  $0.5 \text{ A g}^{-1}$  in 3.0 M KOH. It shows a high rate capability with more than 96.7% capacitance retention even at  $5 \text{ A g}^{-1}$ . In addition, an aqueous/solid-state flexible electrochemical capacitor energy storage device has been successfully fabricated using  $\text{Co}_3\text{O}_4$ @Co-MOF and activated carbon (AC), which displays high capacity and excellent cycling stability.

## RESULTS AND DISCUSSION

The  $\text{Co}_3\text{O}_4$ @Co-MOF composite was synthesized through a one-pot solvothermal method (Fig. 1). The reaction of  $\text{ptcda}$  ( $\text{C}_{24}\text{H}_8\text{O}_6$ ) and cobalt acetate tetrahydrate ( $\text{Co}(\text{CH}_3\text{COO})_2\cdot 4\text{H}_2\text{O}$ ) ( $\text{C}_{24}\text{H}_8\text{O}_6:\text{Co}(\text{CH}_3\text{COO})_2\cdot 4\text{H}_2\text{O} = 1:1$ ) in water at  $100^\circ\text{C}$  for 12 h with a  $\text{C}_{24}\text{H}_8\text{O}_6:\text{NaOH}$  ratio of 1:4 affords leaf-like Co-MOF sheet ( $\text{Co-MOF}$ ,  $\text{Co}_2\text{C}_{24}\text{H}_8\text{O}_6(\text{OH})_4$ ,  $\sim 5 \mu\text{m}$  in width and  $8 \mu\text{m}$  in length), which has been confirmed by scanning electron microscopy (SEM) measurements (see Fig. S1c, d). Keeping the amount of  $\text{C}_{24}\text{H}_8\text{O}_6$  and  $\text{Co}(\text{CH}_3\text{COO})_2\cdot 4\text{H}_2\text{O}$  unchanged, a decrease in the  $\text{C}_{24}\text{H}_8\text{O}_6:\text{NaOH}$  ratio to 1:2 gives a mixture of Co-MOF and untreated  $\text{ptcda}$  ( $\text{Co-MOF} + \text{ptcda}$ ), while an increase in the  $\text{C}_{24}\text{H}_8\text{O}_6:\text{NaOH}$  ratio to 1:6 results in the formation of a composite of  $\text{Co}_3\text{O}_4$  nanocubes and Co-MOF ( $\text{Co}_3\text{O}_4$ @Co-MOF) (Fig. 2a; Fig. S1a, b, e, f). Under the same reaction

conditions, the reaction of  $\text{Co}(\text{CH}_3\text{COO})_2\cdot 4\text{H}_2\text{O}$  and NaOH with a molar ratio of 1:6 without  $\text{ptcda}$  produces  $\text{Co}_3\text{O}_4$  nanocubes (see Fig. S2).

SEM and transmission electron microscopy (TEM) measurements of  $\text{Co}_3\text{O}_4$ @Co-MOF indicate that the  $\text{Co}_3\text{O}_4$  nanocubes with an approximate average size of 50 nm are uniformly dispersed on both sides of Co-MOF (Fig. 2b–d). Fringes with lattice spacings of 0.243 and 0.466 nm for the (311) and (111) faces, respectively, along with the selected area electron diffraction (SAED) pattern, confirm the good crystalline characteristics of the  $\text{Co}_3\text{O}_4$  nanocubes (Fig. 2e, f). The high-angle annular dark-field scanning TEM (HAADF-STEM) combined with elemental mapping measurements reveal that C, O and Co are distributed throughout the entire sheets (Fig. 2g). At the same time, the concentrations of O and Co dispersed on the nanocubes are relatively high. From these results, it was concluded that hybrid  $\text{Co}_3\text{O}_4$  nanocubes were successfully synthesized on the Co-MOF. The color changes from red ( $\text{Co-MOF} + \text{ptcda}$ ), reddish brown ( $\text{Co-MOF}$ ) to black ( $\text{Co}_3\text{O}_4$ @Co-MOF) (see Fig. S3).

X-ray diffraction (XRD) measurements further confirm that the as-prepared composite is composed of Co-MOF and  $\text{Co}_3\text{O}_4$  (JCPDS No. 42–1467) (see Fig. S4). The major diffraction peaks at  $6.2$ ,  $7.1$ ,  $15.3$ ,  $19.3$  and  $22.0^\circ$ , which can be indexed to the (001), (002), (110), (201) and (202) facets, respectively, of the Co-MOF, agree with those reported for the isostructural Zn-MOF with the formula  $\text{Zn}_2(\text{ptcda})\cdot 2\text{H}_2\text{O}$  in the literature [40]. The structure analysis of Co-MOF is displayed in Fig. S5. The  $[\text{CoO}_6]$  octahedral local structure leads to the connection of perylene cores to each other, forming a 3D open framework with a wavy layered structure. The formation of controllable interlayer spacing through the interaction between  $\text{ptcda}$  and  $\text{Co}^{2+}$  is beneficial to ion migration between organic layers. X-ray photoelectron spectroscopy (XPS) was performed to determine the chemical states of the Co, O and C elements of the as-obtained  $\text{Co}_3\text{O}_4$ @Co-MOF (see Figs S6–S8). The Co 2p spectra indicate that there are two types of Co species; the two fitting peaks at 780.6 and 796.3 eV are ascribed to  $\text{Co}^{2+}$ , while another two fitting peaks at 779.3 and 794.5 eV are attributed to  $\text{Co}^{3+}$ . The peaks at 780.6 and 796.3 eV are ascribed to the sum of  $\text{Co}^{2+}$  of  $\text{Co}_3\text{O}_4$  and Co-MOF [41–43]. The O 1s and C 1s spectra of the samples indirectly verified the formation of  $\text{Co}_3\text{O}_4$ @Co-MOF (see Figs S7, S8). In addition, the  $\text{Co}_3\text{O}_4$ @Co-MOF composites exhibit a high Brunauer–Emmett–Teller (BET) surface area of  $453.5 \text{ m}^2 \text{ g}^{-1}$ , which is remarkably larger than those of other samples (BET surface

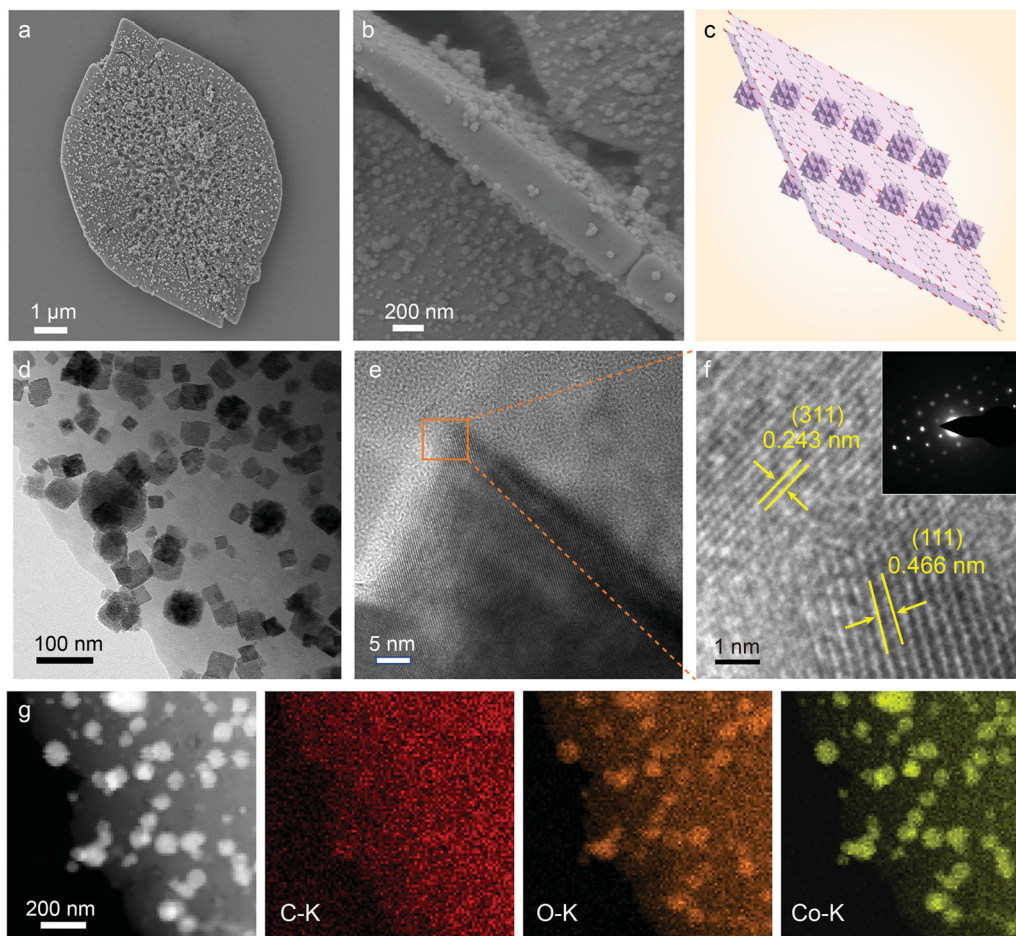


**Figure 2.** Microscopic characterization. (a, b) SEM images, (c) schematic morphology and (d) TEM image of  $\text{Co}_3\text{O}_4@\text{Co-MOF}$ . (e, f) High-resolution transmission electron microscope (HRTEM) images of  $\text{Co}_3\text{O}_4$  (inset of (f): SAED pattern). (g) HAADF-STEM image of  $\text{Co}_3\text{O}_4@\text{Co-MOF}$  and the corresponding elemental mappings of C–K, O–K and Co–K.

areas for Co-MOF + ptcda and Co-MOF are  $313.6$  and  $445.2 \text{ m}^2 \text{ g}^{-1}$ , respectively) (see Fig. S9). As shown in Fig. S10, the pore size distribution for the Barrett–Joyner–Halenda (BJH) adsorption branch implies that the mesopores of the samples were below  $20 \text{ nm}$ . Furthermore, the pore size distribution was calculated through the Saito–Foley (SF) method, finding that the micropores were centered at  $0.5\text{--}1 \text{ nm}$ . These results clearly indicate the coexistence of micropores and mesopores in the samples. Therefore, the samples have a high specific surface area for better electrolyte permeation to access more redox active sites.

The electrochemical capacitive properties of Co-MOF,  $\text{Co}_3\text{O}_4$  and  $\text{Co}_3\text{O}_4@\text{Co-MOF}$  electrodes were evaluated in a three-electrode system in  $3.0 \text{ M KOH}$ . For comparison, we have also mechanically mixed  $\text{Co}_3\text{O}_4$  and Co-MOF together with a mass ratio of 1:4 (the mass ratio calculation process is shown in Figs S11, S12 and Table S2), and the obtained mixture is called ‘ $\text{Co}_3\text{O}_4 + \text{Co-MOF}$ ’ (see Fig. S13). From cyclic voltammetry (CV) curves

of the as-obtained electrodes at different potentials and scan rates, the as-obtained electrodes mainly provide faradaic pseudocapacitive behavior, which is different from that of electric double-layer behavior (see Figs S14, S15) [44,45]. The surrounding area from the CV curve of the  $\text{Co}_3\text{O}_4@\text{Co-MOF}$  is larger than that of the Co-MOF,  $\text{Co}_3\text{O}_4$  and  $\text{Co}_3\text{O}_4 + \text{Co-MOF}$  (Fig. 3a). These redox peaks come largely from the pseudocapacitance produced through faradaic redox reactions. However, the charge storage mechanism of the electrode material is still much less understood at the atomic level. The structural and valence changes of metal oxides/hydroxides during the charge/discharge process have recently been studied by *in situ* and *operando* observations, which offer novel insights into the energy storage mechanism of electrode material [46–48]. It is found that there is no large-scale structural evolution in the process of discharging and charging, but only a few minor migrations or adjustments of atom/ion species. Moreover, the highly reversible conversion of  $\text{Co}_3\text{O}_4/\text{CoOOH}$  can avoid

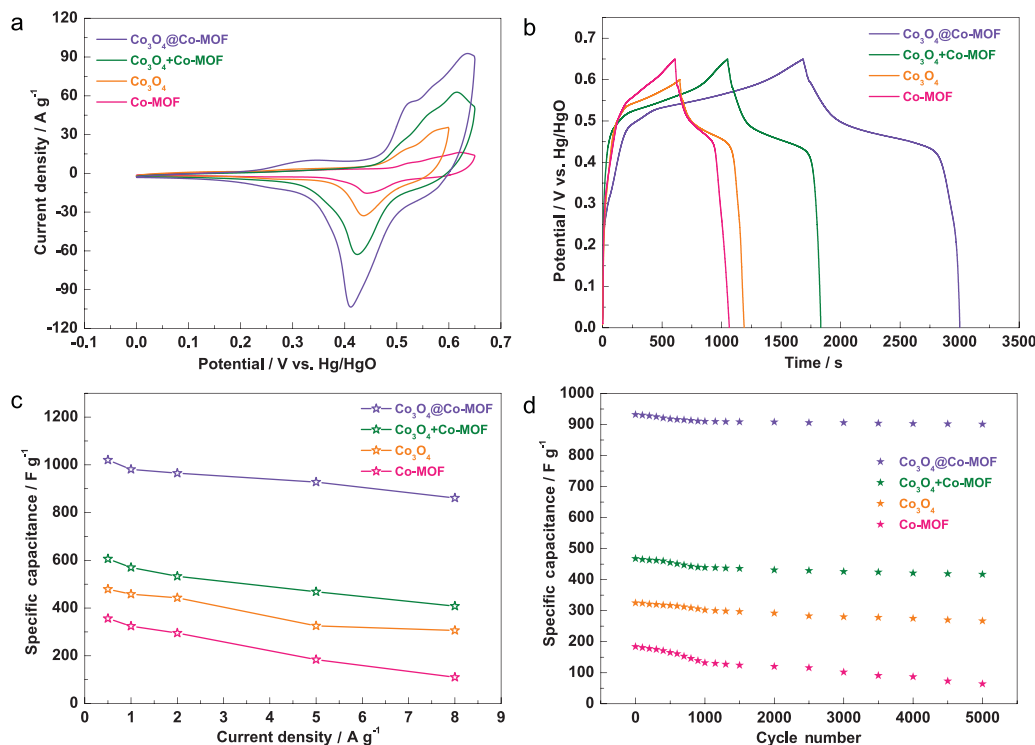
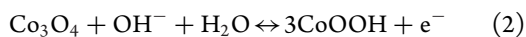
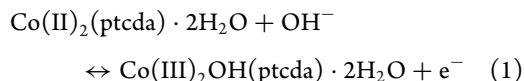


**Figure 3.** Electrochemical results of as-prepared electrodes (Co-MOF,  $\text{Co}_3\text{O}_4$ ,  $\text{Co}_3\text{O}_4 + \text{Co-MOF}$ ,  $\text{Co}_3\text{O}_4@ \text{Co-MOF}$ ) in a three-electrode cell in 3.0 M KOH aqueous solution. (a) CV curves with a scan rate at  $30 \text{ mV s}^{-1}$ . (b) GCD curves at a current density of  $0.5 \text{ A g}^{-1}$ . (c) The specific capacitance changing versus current density from  $0.5 \text{ A g}^{-1}$  to  $8 \text{ A g}^{-1}$ . (d) Cycling performance at  $5 \text{ A g}^{-1}$  for 5000 cycles.

morphological fractures caused by volume changes during cation de-intercalation/intercalation procedures. The possible reaction mechanism for Co-MOF and  $\text{Co}_3\text{O}_4$  is as follows:



To evaluate the electrochemical properties of the as-obtained electrodes, galvanostatic charge-discharge (GCD) curves were generated (Fig. 3b). At  $0.5 \text{ A g}^{-1}$ , the MOF-based materials possess high charge-discharge voltages (0.65 V), which are higher than that of  $\text{Co}_3\text{O}_4$  (0.6 V). In addition, the  $\text{Co}_3\text{O}_4@ \text{Co-MOF}$  displays the longest charge-discharge time. The specific capacitances were calculated from the GCD curves (see Fig. S16) of the as-obtained electrodes at 0.5, 1, 2, 5 and  $8 \text{ A g}^{-1}$  (Fig. 3c; the calculation is shown in the online supporting information). We can see that the specific capacitance of the  $\text{Co}_3\text{O}_4@ \text{Co-MOF}$  composites ( $1020 \text{ F g}^{-1}$ ) is much higher than those of  $\text{Co}_3\text{O}_4 + \text{Co-MOF}$  ( $606 \text{ F g}^{-1}$ ),  $\text{Co}_3\text{O}_4$

( $479 \text{ F g}^{-1}$ ) and Co-MOF ( $356 \text{ F g}^{-1}$ ) at  $0.5 \text{ A g}^{-1}$ , as well as those of the most recently reported metal oxides [49–51], MOFs [12,52,53] and MOF composites [54] (see Tables S3–6). Interestingly, the  $\text{Co}_3\text{O}_4@ \text{Co-MOF}$  offers excellent rate capability through retaining a capacitance of  $861 \text{ F g}^{-1}$  when the current density increases 16 times ( $8 \text{ A g}^{-1}$ ). Even at the current density of  $32 \text{ A g}^{-1}$ , the capacitance can still reach  $469 \text{ F g}^{-1}$  (see Fig. S17), which proves the rate capability of  $\text{Co}_3\text{O}_4@ \text{Co-MOF}$  to be as good as some recently reported high-performance MOF-based materials [46,52,55] (see Table S7). After 5000 cycles, the  $\text{Co}_3\text{O}_4@ \text{Co-MOF}$  decayed only 3.1% compared with its initial capacity. Additionally, large decays were observed for  $\text{Co}_3\text{O}_4 + \text{Co-MOF}$  (10.9%),  $\text{Co}_3\text{O}_4$  (17.8%), and Co-MOF (65.2%) (Fig. 3d). The conductivity of the as-obtained electrodes was also evaluated via electrochemical impedance spectroscopy (EIS) in the frequency range of  $0.01\text{--}10^5 \text{ Hz}$  with open-circuit conditions (see Fig. S18). Moreover, the charge-transfer resistance ( $R_{\text{ct}}$ ) of the electrode was calculated by the Zsimp-Win software. The  $R_{\text{ct}}$  of  $\text{Co}_3\text{O}_4@ \text{Co-MOF}$  was remarkably low, similar to those of  $\text{Co}_3\text{O}_4$ , Co-MOF and  $\text{Co}_3\text{O}_4 + \text{Co-MOF}$ . In addition, the curves showed that the  $R_{\text{ct}}$  after 5000 cycles is marginally larger than that of the

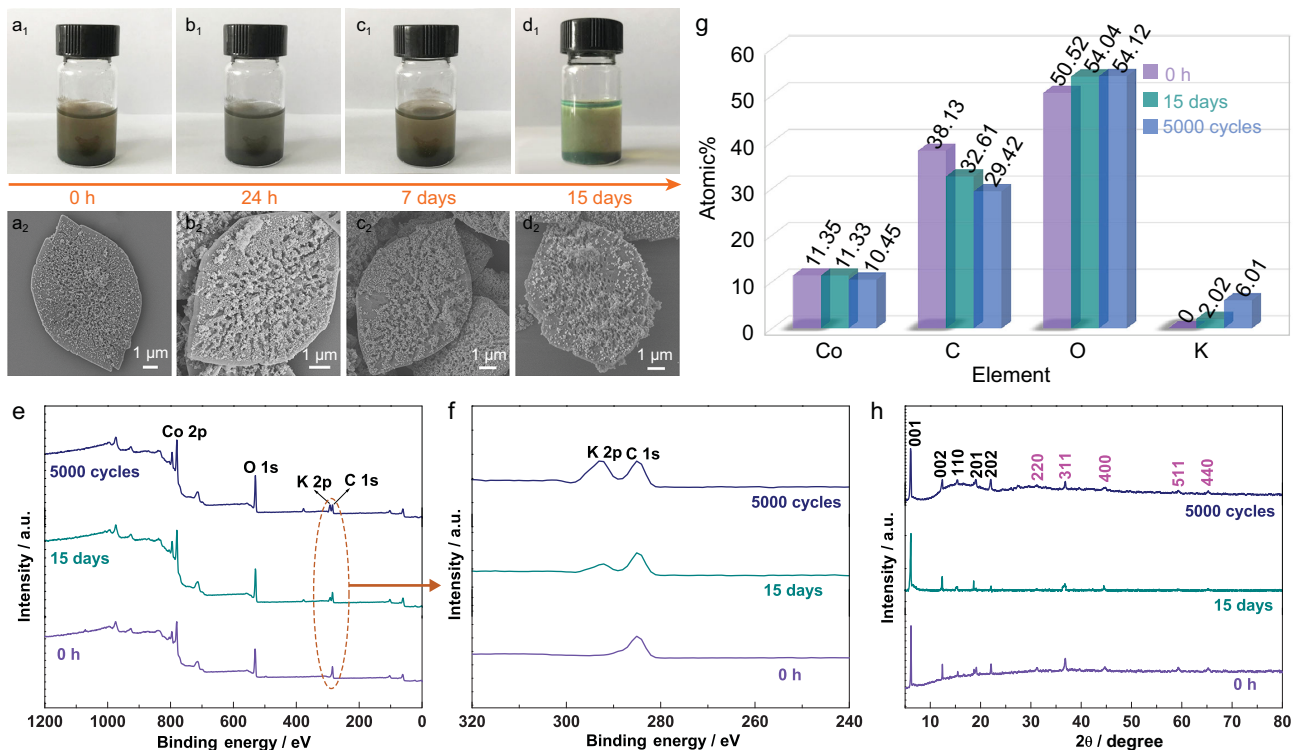


**Figure 4.** (a<sub>1</sub>–d<sub>1</sub>) Optical images of Co<sub>3</sub>O<sub>4</sub>@Co-MOF after immersion in 3.0 M KOH for 0 h, 24 h, 7 days and 15 days. (a<sub>2</sub>–d<sub>2</sub>) The corresponding SEM images. (e, f) XPS spectra and (g) contents of Co, C, O, K. (h) XRD patterns of Co<sub>3</sub>O<sub>4</sub>@Co-MOF for 0 h, 15 days and after cycling for 5000 cycles.

original, which further evidences the stability of the composites.

To further investigate the chemical stabilities and understand the charge–discharge, SEM and TEM images of Co<sub>3</sub>O<sub>4</sub>@Co-MOF after cycling were obtained (see Figs S19–21). The morphology change of Co<sub>3</sub>O<sub>4</sub>@Co-MOF is negligible, and a number of nanopores can be found in the HRTEM image. Furthermore, the corresponding elemental mapping images of Co<sub>3</sub>O<sub>4</sub>@Co-MOF after cycling indicate that the element K was distributed in the entire Co-MOF, which may be due to the occurrence of K<sup>+</sup> intercalation/de-intercalation in the MOF pores during charging/discharging. The chemical stabilities of Co-MOF and Co<sub>3</sub>O<sub>4</sub>@Co-MOF were checked in 3.0 M KOH. Co<sub>3</sub>O<sub>4</sub>@Co-MOF can retain the original morphology after immersion in 3.0 M KOH for 0 h, 24 h, 7 days and 15 days, whereas Co-MOF collapses even after only 24 h (Fig. 4a–d; Figs S22, S23). This is because of the preparation Co<sub>3</sub>O<sub>4</sub>@Co-MOF in strong alkaline conditions of (pH = 11–13) as well as the growth of highly stable Co<sub>3</sub>O<sub>4</sub> on the surface of the Co-MOF, while Co-MOF was formed at pH = 6–8. In addition, Co-MOF is relatively more stable than Co<sub>3</sub>O<sub>4</sub>@Co-MOF in acidic solutions, which may be due to the different synthesis conditions (Figs S24, S25). Further, the XRD patterns and XPS spectra of

Co<sub>3</sub>O<sub>4</sub>@Co-MOF after immersion in the alkaline solution for 0 h and 15 days and after cycling for 5000 cycles show that Co<sub>3</sub>O<sub>4</sub>@Co-MOFs can maintain their framework after cycling and immersion in the alkaline solution, which further confirms their good stability (Fig. 4e, f, h). After immersion and cycling, the element K was found to exist in Co<sub>3</sub>O<sub>4</sub>@Co-MOF, whose at% after cycling was three times that of composites after immersion (Fig. 4g; Fig. S26). Such an interesting phenomenon can be explained by the occurrence of K<sup>+</sup> intercalation/de-intercalation in the MOF pores during charging/discharging and ion exchange in the solution, but for the immersion process, only ion exchange occurs.

Aqueous/solid-state flexible devices were constructed based on positive (the as-prepared nanomaterials) and negative (AC) materials according to the method that we have reported previously (supporting information) [32,54]. The specific capacitance of the activated carbon electrode was 168 F g<sup>−1</sup> at 1.0 A g<sup>−1</sup> (see Fig. S27). Based on the specific capacitance values and potential windows, the mass ratio between the positive and negative electrodes was set at 1:4 in the as-assembled device. In an aqueous electrolyte, the working potential range was expanded to 0–1.55 V (see Figs S28, S29). Figure S31a shows that there is more than one set of redox peaks in the

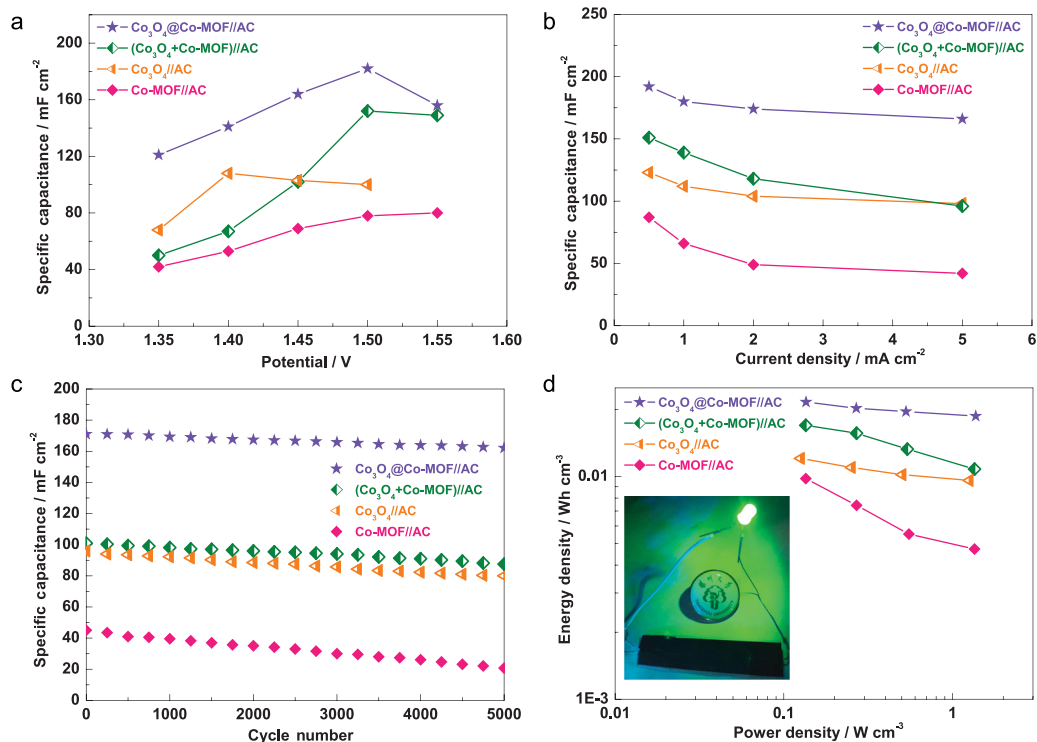


**Figure 5.** Electrochemical measurements of the as-prepared solid-state flexible devices. (a) Specific capacitance change versus potential. (b) Specific capacitance change versus current density. (c) Cycling property at 5  $\text{mA cm}^{-2}$ . (d) Ragone plot exhibiting the relationship between energy density and power density (inset of (d), optical image of the flexible device with solid-state electrolyte).

CV curves, and the CV curves are not rectangular, perhaps because of  $\text{Co}_3\text{O}_4@\text{Co-MOF}$  for the surface redox mechanism of Co (II) to Co (III) from  $\text{Co-MOF}$  and  $\text{Co}_3\text{O}_4$ , respectively. The specific capacitance of the  $\text{Co}_3\text{O}_4@\text{Co-MOF}/\text{AC}$  aqueous device can reach 228  $\text{mF cm}^{-2}$  at 0.5  $\text{mA cm}^{-2}$ , much higher than that of  $\text{Co}_3\text{O}_4 + \text{Co-MOF}/\text{AC}$  (163  $\text{mF cm}^{-2}$ ),  $\text{Co}_3\text{O}_4/\text{AC}$  (129  $\text{mF cm}^{-2}$ ) and  $\text{Co-MOF}/\text{AC}$  (97  $\text{mF cm}^{-2}$ ) (see Figs S30, S31c). Based on the thickness of the electrode (see Fig. S32), the corresponding volumetric capacitances are obtained (Table S3). The specific capacitance of the  $\text{Co}_3\text{O}_4@\text{Co-MOF}/\text{AC}$  aqueous device is 96.2% of its initial capacitance after 5000 cycles (see Fig. S31d), which verifies the superb cycling property. Benefitting from the good conductivity of  $\text{Co}_3\text{O}_4$ , the  $\text{Co}_3\text{O}_4@\text{Co-MOF}/\text{AC}$  aqueous device has a lower  $R_{\text{ct}}$  (see Fig. S33), which agrees well with its good electrochemical property.

The solid-state flexible devices were also constructed via a facile method (see more details in the supporting information). All CV curves of the as-obtained solid-state flexible devices showed obvious oxidation and deoxidation peaks, indicating typical faradaic pseudocapacitive behavior (see Figs S34, S35). Specifically, the CV curves

of the  $\text{Co}_3\text{O}_4@\text{Co-MOF}/\text{AC}$  solid-state flexible device retained their original shapes as the scan rate increased from 5 to 100  $\text{mV s}^{-1}$ , indicating their excellent rate performance. The specific capacitance change versus potential exhibits that the as-prepared MOF-based material solid-state flexible devices have the highest specific capacitance at 1.50 V, whereas, for the  $\text{Co}_3\text{O}_4/\text{AC}$  solid-state flexible device, the highest specific capacitance is located at 1.40 V (Fig. 5a; Fig. S36). The  $\text{Co}_3\text{O}_4@\text{Co-MOF}/\text{AC}$  solid-state flexible device exhibits a high specific capacitance of 192  $\text{mF cm}^{-2}$  at 0.5  $\text{mA cm}^{-2}$ , which is remarkably higher than those of all other devices (specific capacitances for  $\text{Co-MOF}$ ,  $\text{Co}_3\text{O}_4$  and  $\text{Co}_3\text{O}_4 + \text{Co-MOF}$  are 87, 123 and 151  $\text{mF cm}^{-2}$ , respectively) (Fig. 5b; Fig. S37). Interestingly, at 5  $\text{mA cm}^{-2}$ , the  $\text{Co}_3\text{O}_4@\text{Co-MOF}/\text{AC}$  solid-state flexible device provides a superb rate capability via keeping the capacitance of 166  $\text{mF cm}^{-2}$ . After 5000 cycles, only 4.3% of the capacitance of the  $\text{Co}_3\text{O}_4@\text{Co-MOF}/\text{AC}$  solid-state flexible device was lost, which confirms the good cycling ability (Fig. 5c). Moreover, the  $\text{Co}_3\text{O}_4@\text{Co-MOF}/\text{AC}$  solid-state flexible device revealed a low  $R_{\text{ct}}$  value of 17  $\Omega$ , similar to that of  $\text{Co}_3\text{O}_4$  (15  $\Omega$ ). On the other hand,  $\text{Co-MOF}$  exhibited a slightly higher  $R_{\text{ct}}$  value of

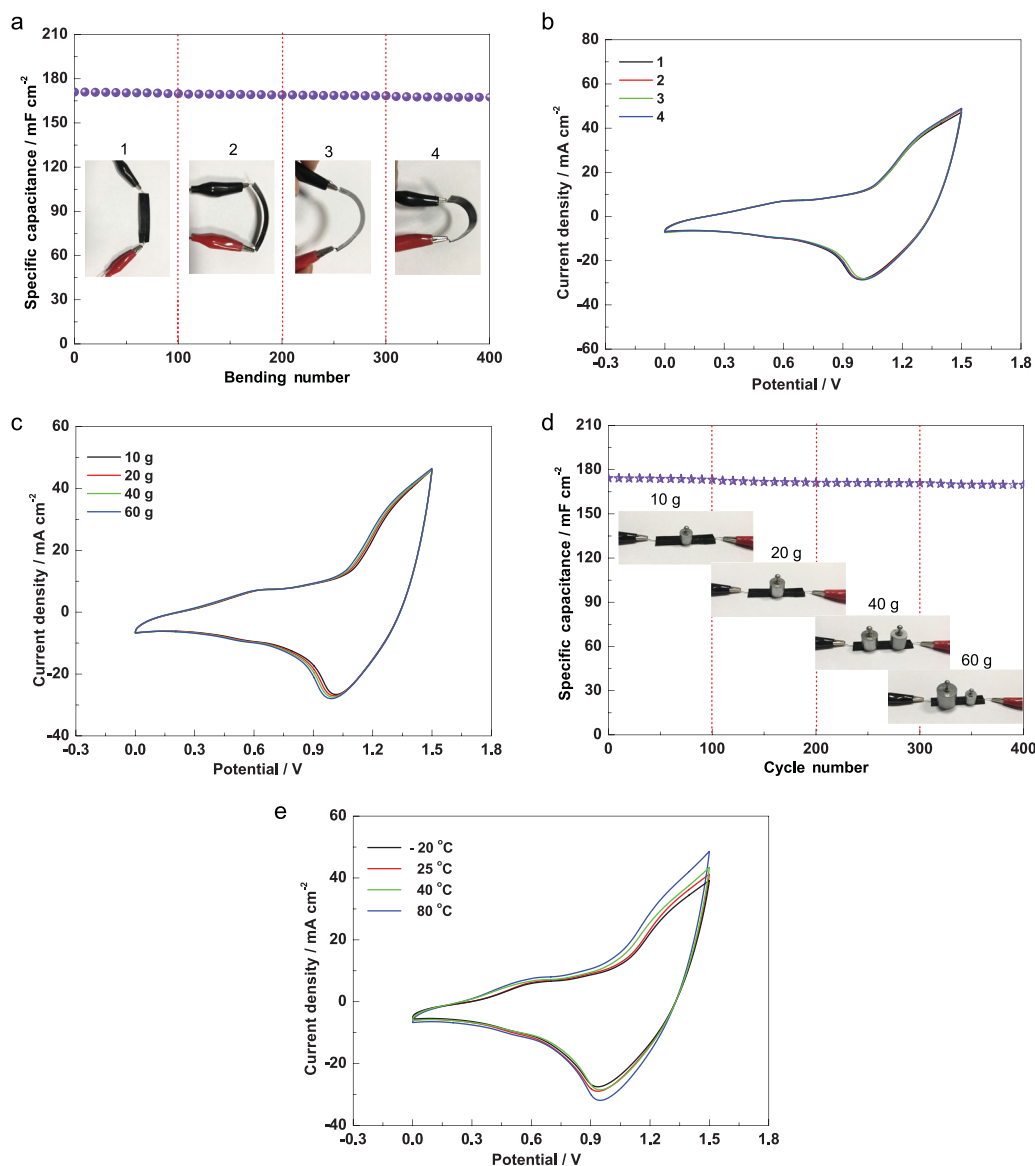


**Figure 6.** Electrochemical flexibility measurements of the as-prepared  $\text{Co}_3\text{O}_4@\text{Co-MOF}/\text{AC}$  solid-state flexible device. (a) Specific capacitance after 400 bending cycles with different bending degrees. (b) CV curves at  $50 \text{ mV s}^{-1}$  with four bending degrees. (c) CV curves under different load pressures. (d) Specific capacitance after 400 cycles under different load pressures. (e) CV curves at different temperatures.

$23 \Omega$  compared with  $\text{Co}_3\text{O}_4@\text{Co-MOF}$ , indicating that the combination of  $\text{Co}_3\text{O}_4$  and Co-MOF effectively improved the electrical conductivity to some extent (see Fig. S38). The power density and energy density are crucial for actual application. The  $\text{Co}_3\text{O}_4@\text{Co-MOF}/\text{AC}$  solid-state flexible device indicated a peak energy density of  $21.6 \text{ mW h cm}^{-3}$  (Fig. 5d). Furthermore, the peak power density of the solid-state flexible device was  $1373.2 \text{ mW cm}^{-3}$  at  $5 \text{ mA cm}^{-2}$ . The maximum energy density of the  $\text{Co}_3\text{O}_4@\text{Co-MOF}/\text{AC}$  solid-state flexible device was larger than those of all other devices. More importantly, the  $\text{Co}_3\text{O}_4@\text{Co-MOF}/\text{AC}$  solid-state flexible device was used to power a green

light-emitting diode (LED). A green LED could be powered for approximately 4 min after charging for 30 s.

To measure the flexibility of the as-fabricated solid-state flexible device, the obtained solid-state flexible device was tested under different bending degrees for every 100 cycles. It is clear that the obtained solid-state flexible device lost only 0.28% under different bending degrees for 400 cycles (Fig. 6a), and TEM images of  $\text{Co}_3\text{O}_4@\text{Co-MOF}$  after 400 bending cycles were obtained (see Fig. S39). The morphology change of  $\text{Co}_3\text{O}_4@\text{Co-MOF}$  is negligible, which further confirms their excellent flexibility and stability. The CV curves under the

four bending degrees are nearly unchanged, which further demonstrates that the obtained solid-state flexible device can work well under flexed conditions (Fig. 6b). Moreover, the environmental stability of the device was also examined by applying different pressures to the device. The CV curves with different load weights from 10 to 60 g change slightly (Fig. 6c). In the meantime, the obtained solid-state flexible device was tested under different load pressures for every 100 cycles, and the device demonstrated only 0.22% loss under different load pressures after 400 cycles (Fig. 6d). The device was measured at different temperatures from  $-20$  to  $80^{\circ}\text{C}$ , but the area under the CV curve did not change much (Fig. 6e). Compared with that at room temperature ( $25^{\circ}\text{C}$ ), the area under the CV curve mildly increased at  $80^{\circ}\text{C}$ , while it very slightly decreased at  $-20^{\circ}\text{C}$ . The reason for this might be the increased ion transport rate at elevated temperatures. When the temperature is higher than  $80^{\circ}\text{C}$ , the solid-state electrolyte changes into gel electrolyte, and thus we choose  $80^{\circ}\text{C}$  as the highest temperature.

## CONCLUSIONS

In summary, a composite of cobalt oxide nanocubes on Co-MOF sheet ( $\text{Co}_3\text{O}_4@\text{Co-MOF}$ ) was successfully synthesized via a one-pot hydrothermal reaction under highly alkaline conditions. Without hybridizing with  $\text{Co}_3\text{O}_4$ , Co-MOF can provide an appropriate space for the electrochemical reaction and intercalation/de-intercalation of  $\text{K}^+$  during the energy storage process, but the alkaline stability of pristine Co-MOF is poor, resulting in capacitance as low as  $356\text{ F g}^{-1}$ . The presence of  $\text{Co}_3\text{O}_4$  on the surface of Co-MOF effectively improves the alkaline stability, increases redox active sites, leading to dramatic enhancement of capacitance to  $1020\text{ F g}^{-1}$  at  $0.5\text{ A g}^{-1}$ . Such a highly alkaline-stable  $\text{Co}_3\text{O}_4@\text{Co-MOF}$  composite shows significant advantages for application as an electrochemical capacitor energy storage device electrode in terms of enhanced durability and capacitance. The  $\text{Co}_3\text{O}_4@\text{Co-MOF}$  composite shows a high cycling stability after 5000 cycles with only 3.3% decay at  $5\text{ A g}^{-1}$ . More remarkably, the as-constructed aqueous/solid-state device showed high specific capacitance, wonderful cycle stability and high energy density. In addition, the as-fabricated solid-state flexible device showed excellent mechanical flexibility and environmental stability. Considering the merits of the facile synthetic method, simple construction and outstanding properties, the  $\text{Co}_3\text{O}_4@\text{Co-MOF}//\text{AC}$  solid-state flexible device opens up bright prospects in portable, flexible and lightweight electronic applications.

## SUPPLEMENTARY DATA

Supplementary data are available at [NSR](#) online.

## ACKNOWLEDGEMENTS

We acknowledge the Priority Academic Program Development of Jiangsu Higher Education Institutions and the technical support that we received at the Testing Center of Yangzhou University.

## FUNDING

This work was supported by the National Natural Science Foundation of China (21671170, 21875207 and 21673203), the Top-notch Academic Programs Project of Jiangsu Higher Education Institutions, the Program for New Century Excellent Talents of the University in China (NCET-13-0645), the Six Talent Plan (2015-XCL-030) and the Qinglan Project.

**Conflict of interest statement.** None declared.

## REFERENCES

1. Yaghi OM, Li G and Li H. Selective binding and removal of guests in a microporous metal-organic framework. *Nature* 1995; **378**: 703–6.
2. Rosi NL, Kim J and Eddaoudi M *et al.* Rod packings and metal-organic frameworks constructed from rod-shaped secondary building units. *J Am Chem Soc* 2005; **127**: 1504–18.
3. Shen K, Zhang L and Chen X *et al.* Ordered macro-microporous metal-organic framework single crystals. *Science* 2018; **359**: 206–10.
4. Li J, Wang X and Zhao G *et al.* Metal-organic framework-based materials: superior adsorbents for the capture of toxic and radioactive metal ions. *Chem Soc Rev* 2018; **47**: 2322–56.
5. Jeong GY, Singh AK and Kim MG *et al.* Metal-organic framework patterns and membranes with heterogeneous pores for flow-assisted switchable separations. *Nat Commun* 2018; **9**: 3968.
6. Chen CX, Wei ZW and Jiang JJ *et al.* Dynamic spacer installation for multirole metal-organic frameworks: a new direction toward multifunctional MOFs achieving ultrahigh methane storage working capacity. *J Am Chem Soc* 2017; **139**: 6034–7.
7. Yang W, Li X and Li Y *et al.* Applications of metal-organic-framework-derived carbon materials. *Adv Mater* 2018; **31**: 1804740.
8. Chen YZ, Wang ZU and Wang H *et al.* Singlet oxygen-engaged selective photo-oxidation over Pt nanocrystals/porphyrinic MOF: the roles of photothermal effect and Pt electronic state. *J Am Chem Soc* 2017; **139**: 2035–44.
9. Yang Q, Xu Q and Jiang HL. Metal-organic frameworks meet metal nanoparticles: synergistic effect for enhanced catalysis. *Chem Soc Rev* 2017; **46**: 4774–808.
10. Yang X, Sun JK and Kitta M *et al.* Encapsulating highly catalytically active metal nanoclusters inside porous organic cages. *Nat Catal* 2018; **1**: 214–20.
11. Zhao S, Wang Y and Dong J *et al.* Ultrathin metal-organic framework nanosheets for electrocatalytic oxygen evolution. *Nat Energy* 2016; **1**: 16184.



12. Sheberla D, Bachman JC and Elias JS *et al.* Conductive MOF electrodes for stable supercapacitors with high areal capacitance. *Nat Mater* 2017; **16**: 220–4.
13. Wang L, Feng X and Ren L *et al.* Flexible solid-state supercapacitor based on a metal-organic framework interwoven by electrochemically-deposited PANI. *J Am Chem Soc* 2015; **137**: 4920–3.
14. Wang Y, Song Y and Xia Y. Electrochemical capacitors: mechanism, materials, systems, characterization and applications. *Chem Soc Rev* 2016; **45**: 5925–50.
15. Jiang H, Liu XC and Wu Y *et al.* Metal-organic frameworks for high charge-discharge rates in lithium-sulfur batteries. *Angew Chem Int Ed* 2018; **57**: 3916–21.
16. Wang L, Han Y and Feng X *et al.* Metal-organic frameworks for energy storage: batteries and supercapacitors. *Coord Chem Rev* 2016; **307**: 361–81.
17. Wang HL, Zhu QL and Zou RQ *et al.* Metal-organic frameworks for energy applications. *Chem* 2017; **2**: 52–80.
18. Zheng SS, Li XR and Yan BY *et al.* Transition-metal (Fe, Co, Ni) based metal-organic frameworks for electrochemical energy storage. *Adv Energy Mater* 2017; **7**: 1602733.
19. Lu XF, Liao PQ and Wang JW *et al.* An alkaline-stable, metal hydroxide mimicking metal-organic framework for efficient electrocatalytic oxygen evolution. *J Am Chem Soc* 2016; **138**: 8336–9.
20. Zheng SS, Xue HG and Pang H. Supercapacitors based on metal coordination materials. *Coord Chem Rev* 2018; **373**: 2–21.
21. Yi FY, Zhang R and Wang H *et al.* Metal-organic frameworks and their composites: synthesis and electrochemical applications. *Small Methods* 2017; **1**: 1700187.
22. Dou S, Song J and Xi S *et al.* Boosting electrochemical CO<sub>2</sub> reduction on metal-organic frameworks via ligand doping. *Angew Chem Int Ed* 2019; **58**: 4041–5.
23. Kim SH, Lee HH and Kim JM *et al.* Heteromat-framed metal-organic coordination polymer anodes for high-performance lithium-ion batteries. *Energy Storage Mater* 2019; **19**: 130–6.
24. Wang Q and O'Hare D. Recent advances in the synthesis and application of layered double hydroxide (LDH) nanosheets. *Chem Rev* 2012; **112**: 4124–55.
25. Jiang J, Li Y and Liu J *et al.* Recent advances in metal oxide-based electrode architecture design for electrochemical energy storage. *Adv Mater* 2012; **24**: 5166–80.
26. Li X, Wei J and Li Q *et al.* Nitrogen-doped cobalt oxide nanostructures derived from cobalt-alanine complexes for high-performance oxygen evolution reactions. *Adv Funct Mater* 2018; **28**: 1800886.
27. Chen LF, Yu ZY and Wang JJ *et al.* Metal-like fluorine-doped  $\beta$ -FeOOH nanorods grown on carbon cloth for scalable high-performance supercapacitors. *Nano Energy* 2015; **11**: 119–28.
28. Zhai T, Wan L and Sun S *et al.* Phosphate ion functionalized Co<sub>3</sub>O<sub>4</sub> ultrathin nanosheets with greatly improved surface reactivity for high performance pseudocapacitors. *Adv Mater* 2017; **29**: 1604167.
29. Li B, Gu P and Feng Y *et al.* Ultrathin nickel-cobalt phosphate 2D nanosheets for electrochemical energy storage under aqueous/solid-state electrolyte. *Adv Funct Mater* 2017; **27**: 1605784.
30. Grote F, Yu ZY and Wang JL *et al.* Self-stacked reduced graphene oxide nanosheets coated with cobalt-nickel hydroxide by one-step electrochemical deposition toward flexible electrochromic supercapacitors. *Small* 2015; **11**: 4666–72.
31. Gao S, Sun Y and Lei F *et al.* Ultrahigh energy density realized by a single-layer  $\beta$ -Co(OH)<sub>2</sub> all-solid-state asymmetric supercapacitor. *Angew Chem Int Ed* 2014; **53**: 12789–93.
32. Liao Q, Li N and Jin S *et al.* All-solid-state symmetric supercapacitor based on Co<sub>3</sub>O<sub>4</sub> nanoparticles on vertically aligned graphene. *ACS Nano* 2015; **9**: 5310–7.
33. Zhan W, Kuang Q and Zhou J *et al.* Semiconductor@metal-organic framework core-shell heterostructures: a case of ZnO@ZIF-8 nanorods with selective photoelectrochemical response. *J Am Chem Soc* 2013; **135**: 1926–33.
34. Zhu QL and Xu Q. Metal-organic framework composites. *Chem Soc Rev* 2014; **43**: 5468–512.
35. Wei T, Zhang M and Wu P *et al.* POM-based metal-organic framework/reduced graphene oxide nanocomposites with hybrid behavior of battery-supercapacitor for superior lithium storage. *Nano Energy* 2017; **34**: 205–14.
36. Hu X, Shao W and Hang X *et al.* Superior electrical conductivity in hydrogenated layered ternary chalcogenide nanosheets for flexible all-solid-state supercapacitors. *Angew Chem Int Ed* 2016; **128**: 5827–32.
37. Yang J, Zhang F and Lu H *et al.* Hollow Zn/Co ZIF particles derived from core-shell ZIF-67@ZIF-8 as selective catalyst for the semi-hydrogenation of acetylene. *Angew Chem Int Ed* 2015; **54**: 10889–93.
38. Yu J, Mu C and Yan B *et al.* Nanoparticle/MOF composites: preparations and applications. *Mater Horizons* 2017; **4**: 557–69.
39. Lian X, Fang Y and Joseph E *et al.* Enzyme-MOF (metal-organic framework) composites. *Chem Soc Rev* 2017; **46**: 3386–401.
40. Zhao J, Li M and Sun J *et al.* Metal-oxide nanoparticles with desired morphology inherited from coordination-polymer precursors. *Chem Eur J* 2012; **18**: 3163–8.
41. Xu L, Jiang Q and Xiao Z *et al.* Plasma-engraved Co<sub>3</sub>O<sub>4</sub> nanosheets with oxygen vacancies and high surface area for the oxygen evolution reaction. *Angew Chem Int Ed* 2016; **55**: 5277–81.
42. Zhao L, Dong B and Li S *et al.* Interdiffusion reaction-assisted hybridization of two-dimensional metal-organic frameworks and Ti<sub>3</sub>C<sub>2</sub>T<sub>x</sub> nanosheets for electrocatalytic oxygen evolution. *ACS Nano* 2017; **11**: 5800–7.
43. Wang Y, Zhou T and Jiang K *et al.* Reduced mesoporous Co<sub>3</sub>O<sub>4</sub> nanowires as efficient water oxidation electrocatalysts and supercapacitor electrodes. *Adv Energy Mater* 2014; **4**: 1400696.
44. Zhai T, Sun S and Liu X *et al.* Achieving insertion-like capacity at ultrahigh rate via tunable surface pseudocapacitance. *Adv Mater* 2018; **30**: 1706640.
45. Wang J, Xu Y and Ding B *et al.* Confined self-assembly in two-dimensional interlayer space: monolayered mesoporous carbon nanosheets with in-plane orderly arranged mesopores and a highly graphitized framework. *Angew Chem Int Ed* 2018; **57**: 2894–8.
46. Deng T, Lu Y and Zhang W *et al.* Inverted design for high-performance supercapacitor via Co(OH)<sub>2</sub>-derived highly oriented MOF electrodes. *Adv Energy Mater* 2018; **8**: 1702294.
47. Li HB, Yu MH and Wang FX *et al.* Amorphous nickel hydroxide nanospheres with ultrahigh capacitance and energy density as electrochemical pseudocapacitor materials. *Nat Commun* 2013; **4**: 1894.
48. Deng T, Zhang W and Arcelus O *et al.* Atomic-level energy storage mechanism of cobalt hydroxide electrode for pseudocapacitors. *Nat Commun* 2017; **8**: 15194.
49. Meng F, Fang Z and Li Z *et al.* Porous Co<sub>3</sub>O<sub>4</sub> materials prepared by solid-state thermolysis of a novel Co-MOF crystal and their superior energy storage performances for supercapacitors. *J Mater Chem A* 2013; **1**: 7235.

50. Chen S, Xue M and Li Y *et al.* Rational design and synthesis of  $\text{Ni}_x\text{Co}_{3-x}\text{O}_4$  nanoparticles derived from multivariate MOF-74 for supercapacitors. *J Mater Chem A* 2015; **3**: 20145–52.
51. Zhang YZ, Wang Y and Xie YL *et al.* Porous hollow  $\text{Co}_3\text{O}_4$  with rhombic dodecahedral structures for high-performance supercapacitors. *Nanoscale* 2014; **6**: 14354–9.
52. Qu C, Jiao Y and Zhao B *et al.* Nickel-based pillared MOFs for high-performance supercapacitors: design, synthesis and stability study. *Nano Energy* 2016; **26**: 66–73.
53. Yan Y, Gu P and Zheng SS *et al.* Facile synthesis of an accordion-like Ni-MOF superstructure for high-performance flexible supercapacitors. *J Mater Chem A* 2016; **4**: 19078–85.
54. Zhang YZ, Cheng T and Wang Y *et al.* Flexible supercapacitors: a simple approach to boost capacitance: flexible supercapacitors based on manganese oxides@MOFs via chemically induced in situ self-transformation. *Adv Mater* 2016; **28**: 5241.
55. Yang J, Zheng C and Xiong P *et al.* Zn-doped Ni-MOF material with a high supercapacitive performance. *J Mater Chem A* 2014; **2**: 19005–10.